Nanocomposite TiSiN coatings deposited by large area filtered arc deposition

Y. H. Cheng, T. Browne, and B. Heckerman

Articles you may be interested in

Microstructure and tribological performance of nanocomposite Ti–Si–C–N coatings deposited using hexamethyldisilazane precursor
J. Vac. Sci. Technol. A **28**, 1126 (2010); 10.1116/1.3463709

TiCN coatings deposited by large area filtered arc deposition technique
J. Vac. Sci. Technol. A **28**, 431 (2010); 10.1116/1.3372403

Synthesis and characteristics of new quaternary Ti–Mo–Si–N coatings by a hybrid coating system
J. Vac. Sci. Technol. A **26**, 140 (2008); 10.1116/1.2821730

Effect of oxygen incorporation on structural and properties of Ti–Si–N nanocomposite coatings deposited by reactive unbalanced magnetron sputtering
J. Vac. Sci. Technol. A **24**, 974 (2006); 10.1116/1.2202128

Structural characterization of nanocomposite Ti–Si–N coatings prepared by pulsed dc plasma-enhanced chemical vapor deposition
J. Vac. Sci. Technol. B **22**, 1694 (2004); 10.1116/1.1763593

Nanocomposite TiSiN coatings deposited by large area filtered arc deposition

Y. H. Cheng,[a)] T. Browne, and B. Heckerman
American Eagle Instruments, Inc., 6575 Butler Creek Rd., Missoula, Montana 59808

Nanocomposite TiSiN coatings were successfully synthesized at a temperature and N_2 partial pressure of 350 °C and 0.02 Pa, respectively, from TiSi alloy targets with Si content of 20 at. % by using a large area filtered arc deposition technique. Scanning electron microscopy, x-ray diffraction (XRD), and x-ray photoelectron spectroscopy (XPS) were used to investigate the surface morphology, crystalline structure, grain size, composition, and bonding structure of the deposited coatings. Nanoindentation was used to characterize the mechanical properties of the deposited coatings. It was found that adding Si into TiN coatings reduces the grain size significantly from 16.9 to 5.8 nm, changes the orientation from (111) to (220) preferred orientation, and increases the hardness and Young's modulus from 33 and 376 GPa to 51 and 449 GPa, respectively. XPS and XRD results show that the Si/Ti atomic ratio in the coatings is 0.17 and the deposited TiSiN coatings consist of nanosized TiN grains encapsulated by amorphous Si_3N_4 layer, corresponding to the superhigh hardness of the TiSiN coatings. The high plasma density, ion energy, and ion reactivity of the filtered cathodic arc plasma contribute to the formation of the nanocomposite TiSiN coatings at low temperature and low N_2 partial pressure. © *2009 American Vacuum Society.*
[DOI: 10.1116/1.3043460]

I. INTRODUCTION

Nanocomposite coatings, consisting of nanosized (3–20 nm) crystallites of transition metal nitrides (nc-MeN) embedded in an amorphous Si, B, and/or C nitride matrix, have gained significant attention due to their unusual and unique properties.[1–4] The small dimension of the crystallites prevents the nucleation and propagation of dislocations inside the nanocrystallites. The deformation of the coatings is governed by grain boundary sliding. When the thickness of the amorphous phase is reduced to a few atoms thick, the grain boundary sliding is also inhibited. As a result, these nanocomposite coatings possess ultrahigh hardness (>40 GPa). In addition, as the nanocrystallites prevent the movement of the crack, the crack propagation inside the nanocomposite undergoes bending and branching, which increases the coating toughness.

nc-TiN/a-Si_3N_4 coating is a nanocomposite coating and has been extensively studied in recent years. In addition to the high hardness, the Ti–Si–N coatings also possess excellent corrosion resistance, high thermal stability of the nanostructure, high hardness at high temperature, and excellent oxidization resistance due to the formation of a dense SiO_2 protective layer under high temperature and oxidative environment.[2–5] The combination of these unique properties makes the TiSiN coating an ideal candidate for many applications.

Ti–Si–N nanocomposite coatings have been synthesized by using chemical vapor deposition,[2–4] plasma enhanced chemical vapor deposition,[5] magnetron sputtering,[6] and cathodic vacuum arc.[7,8] Among them, cathodic vacuum arc is one of the most suitable techniques for large scale and high volume industry deposition due to its high ion energy, high ionization rate, and high deposition rate. However, the macroparticles formed during the cathodic arc evaporation degrade the coating properties, especially the corrosion resistance and wear resistance. Our patented large area filtered cathodic arc deposition (LAFAD) technique utilizes 90° deflecting magnetic fields to deflect ions from the cathodic arc plasma to the deposition chamber and removes the unwanted macroparticles generated during arc evaporation.[9–12] Utilizing focusing magnetic fields, for a source with a window of 20×40 cm^2, extremely high ion currents, 4 A, are obtained with ionization efficiencies approaching nearly 100%. This capability results in a highly productive deposition process. Manipulation of the arc plasma jets using strategically placed scanning magnetic coils and auxiliary anodes creates a "plasma-immersion" environment in the coating chamber, substantially reduces the shadowing effect that causes non-uniform coating thickness when complex, three-dimensionally shaped substrates are coated in conventional deposition systems.

In this study, nanocomposite TiSiN coatings were deposited from TiSi alloy targets using LAFAD technique. The surface morphology, composition, bonding structure, crystalline structure, hardness, Young's modulus, and plasticity of the deposited coatings were characterized using scanning electron microscopy (SEM), x-ray photoelectron spectroscopy (XPS), x-ray diffraction (XRD), and nanoindentation. As a reference, TiN coatings deposited using the same system were also systematically studied.

[a)]Electronic addresses: yh_cheng@yahoo.com or ycheng@am-eagle.com

II. EXPERIMENT

A LAFAD-1 surface engineering system was used to deposit TiSiN nanocomposite coatings. The detailed description of the deposition system was published in a previous paper.[13] Briefly, this system consists of one dual filtered arc source, one rectangular plasma-guide chamber, one deposition chamber, auxiliary anodes, heating system, substrate bias system, and vacuum system. The dual filtered arc source consists of two primary cathodic arc sources utilizing round TiSi targets, which are placed opposite to each other on the sidewalls of the plasma-guide chamber, surrounded by rectangular deflecting coils, and separated by an anodic baffle plate. The deposition temperature was controlled by heating elements. The deposition zone for this system is about 50 cm diameter $\times$ 30 cm high. Mirror finished 17-4 stainless coupons with a size of $\phi 12.5 \times 3$ mm^2 were used as substrates for characterizing the crystalline structure and internal stress in the coatings, respectively.

The substrates were thoroughly cleaned and dried using an ultrasonic cleaning system before loading into the deposition chamber. Before deposition, the coupons were subjected to Ar plasma cleaning at a pressure, temperature, bias, and time of 0.08 Pa, 350 °C, −250 V, and 15 min, respectively, followed by the Ti ion subimplantation at a pressure, bias, and time of 0.02 Pa, 500 V, and 2 min, respectively. In order to improve the adhesion of the TiSiN coatings, a TiSi–TiSiN gradient multilayer with a thickness of about 200 nm was deposited onto the coupon surface. The gradient layer was deposited by gradually increasing N$_2$ content in the chamber from 0% to 100%. After the deposition of the compositional gradient bonding layer, TiSiN coatings with a thickness of 2.5 μm were deposited.

The surface morphology of the TiSiN coatings was observed using a Hitachi S-4700 field emission SEM at the EMtrix Electron Microscopy Center, University of Montana. The SEM was operated at 20 kV.

The phase structure and grain size of the TiSiN nanocomposite coatings were studied using a Siemens D500 x-ray diffractometer with a Cu $K\alpha$ radiation source (λ = 0.154 06 nm). The accelerating voltage and filament current were 40 kV and 30 mA, respectively.

The composition and bonding structure of the TiSiN coatings were investigated using a XPS instrument (PHI Model 5600ci, CASA XPS analytical software). A monochromatic Al $K\alpha$ x-ray source was used for all samples. The conditions used for the survey scans were as follows: energy range, 1100–0 eV; pass energy, 160 eV; step size, 0.7 eV; sweep time, 180 s; and x-ray spot size, 700×400 μm^2. For the high-resolution spectra, an energy range of 40–20 eV was used, depending on the peak being examined, with a pass energy of 10 eV and a step size of 0.05 eV.

Nanoindentation tests were conducted using a MTS Nano Indenter® XP (MTS Systems Corp., Oak Ridge, TN, USA) with a Berkovich diamond tip. Hardness and elastic moduli were measured using the continuous stiffness measurement option. Si was used as a standard sample for the initial calibration. In the present study, a typical indentation experiment
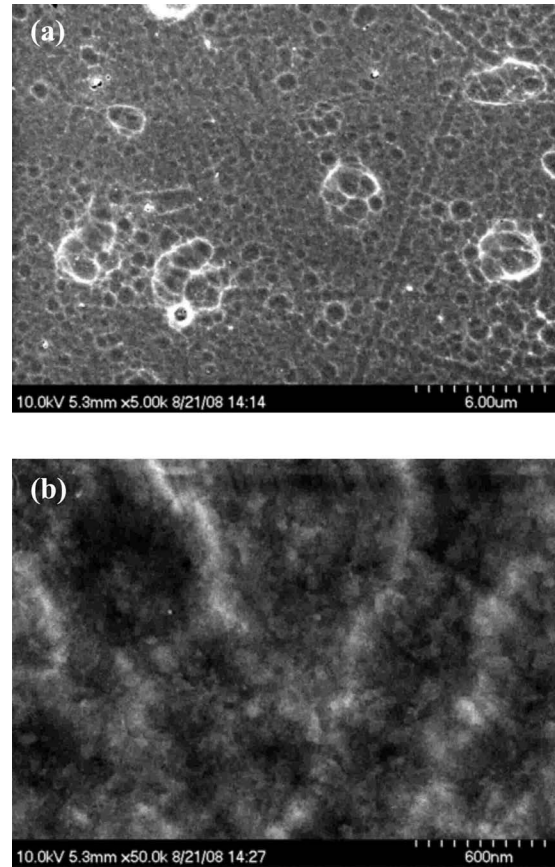
FIG. 1. Typical surface morphology of the TiSiN coating deposited by LAFAD.

consists of seven subsequent steps: approaching the surface; determining the contact point; loading to peak load; holding the tip for 10 s at the peak load; unloading 90% of peak load; holding the tip for 30 s at 10% of the peak load for thermal drift correction; and finally unloading completely. The experimental parameters were chosen as follows: strain rate, 0.05 s^{-1}; allowable thermal drift rate, 0.05 nm/s; depth limit, 1.5 μm. The hardness and elastic modulus were obtained from the curves using the Oliver-Pharr method.

III. RESULTS

The surface morphology of the TiSiN and TiN coatings were observed by using scanning electron microscopy. Figure 1 exhibits the typical morphology of the TiSiN coating. The surface morphology of the TiN coating was shown in a previous report, which showed that the deposited TiN coatings consist of spherical shaped clusters with a size of about 50–200 nm, which are uniformly distributed on the coating surface. However, the TiSiN coatings exhibit a completely different morphology. As shown in Fig. 1(a), multiple circular craters with a size of 0.2–2 μm can be observed on the TiSiN coating surface. High magnification SEM image, Fig. 1(b), shows that the craters are comprised of nanosized clusters with a size of 35–150 nm, which is much smaller than the cluster size on the TiN coating surface. These nanosized
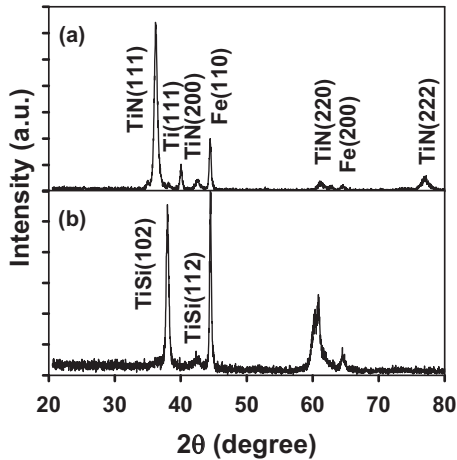
FIG. 2. XRD patterns of the (a) TiN and (b) TiSiN coatings on stainless steel.

FIG. 3. XPS survey spectra of TiSiN coatings on stainless steel (a) before and (b) after ion sputtering.

clusters are self-assembled and form concave craters. The detailed mechanism for the formation of the clusters is not clear and needs further research.

The phase structure and grain size of the TiN and TiSiN coatings were investigated by XRD in the 2θ range of $20°-80°$ with a θ-2θ scan. Figure 2 shows the typical XRD patterns of the (a) TiN and (b) TiSiN coatings on 17-4 stainless steel substrates. For the TiN coatings, four peaks corresponding to the (111), (200), (220), and (222) planes of the cubic TiN phase appear except for the peaks from the Ti bonding layer and steel substrate. The (111) peak exhibits the highest intensity, indicating that the deposited TiN coatings exhibit very strong (111) preferred orientation. Five diffraction peaks at 2θ angles of 38.00°, 42.32°, 44.50°, 60.64°, and 64.50°, can be observed in the XRD patterns from TiSiN coatings. According to Ref. 14, the first and second peaks correspond to the (102) and (112) planes of the Si_3Ti_5 phase with a hexagonal structure. Our previous analysis shows that the third and fifth peaks correspond to the (110) and (200) planes of the steel substrate. After comparing with Ref. 15, it can be concluded that the fourth peak corresponds to the (220) plane of the cubic TiN phase, indicating that the deposited TiSiN coatings possess a cubic NaCl-type crystalline structure and exhibit a completely (220) preferred orientation. No diffraction peaks originating from any SiN_x phases can be observed from the XRD patterns of the TiSiN coatings, indicating that the SiN_x phase in the coating is amorphous or at least XRD amorphous.

In addition, it is worth noting that the (220) peak of the TiSiN coating is very broad, indicating the very small grain size in the coatings. After fitting the XRD peaks with the Gaussian function, it was found that the full width at half maximum (FWHM) of the TiN (111) peak and the TiSiN (220) peak are 0.49° and 1.58°, respectively. By using the Scherer equation, the grain sizes in TiN and TiSiN coatings were calculated to be 16.9 and 5.8 nm, respectively. Clearly, the addition of Si into TiN coatings results in a significant
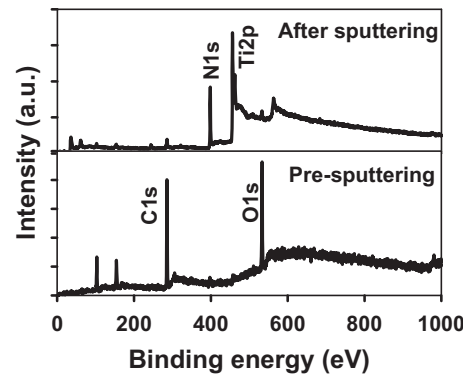
reduction in the grain size. This is consistent with the SEM observations, which show a reduction in the cluster size after adding Si into the TiN coating.

Although the crystallographic phase structure of the crystalline coatings can be studied using XRD, it is difficult to characterize the phase and bonding structure of the multiphase nanocomposite coatings in which the amorphous phase, minor nanosized phase, or very thin phases between the grains exist, but are not detectable by XRD. It is very important to characterize the nanocomposite TiSiN coatings using XPS, which is a highly sensitive and nondestructive technique used for characterizing the composition and bonding structures of materials. Figure 3 shows the typical XPS survey scan spectra of TiSiN coatings on stainless steel before and after Ar plasma sputtering cleaning. Before plasma sputtering, only two strong peaks from C 1s and O 1s peaks can be detected. After sputtering, using Ar plasma at a bias of 3 kV for 5 min, the C 1s and O 1s peak intensities decrease dramatically to a negligible level. This implies that the strong C 1s and O 1s peaks come from the contamination of the coating surface during the exposure of the coating to the air. Meanwhile, two strong peaks, originated from N 1s and Ti 2p, appear in the XPS spectrum of the TiSiN coating after plasma cleaning.

To quantify the composition and the bonding structure of the TiSiN coatings, high-resolution spectra of Ti 2p, N 1s, Si 2p, C 1s, and O 1s were collected and fitted using the Gaussian function, as shown in Fig. 4. All spectra were calibrated using the adventitious C 1s peak with a fixed value of 284.6 eV. The background from each spectrum was subtracted and the area under each peak was used to calculate the composition of the TiSiN coatings using relative sensitivity factors from the manufacturer's handbook: Ti (1.798), N (0.477), Si (0.283), C (0.296), and O (0.711). The atomic contents of Ti, N, Si, C, and O were calculated to be 36.46%, 37.36%, 6.16%, 12.76%, and 7.26%, respectively. The atomic ratio of Si over Ti is 0.17, which is slightly lower than the Si/Ti content (0.25) in the targets. This may be caused by the difference in the ionization rate, charging, and the emission energy of Si and Ti atoms in the arc plasma, which significantly affects the transportation of ions in the magnetic filter.
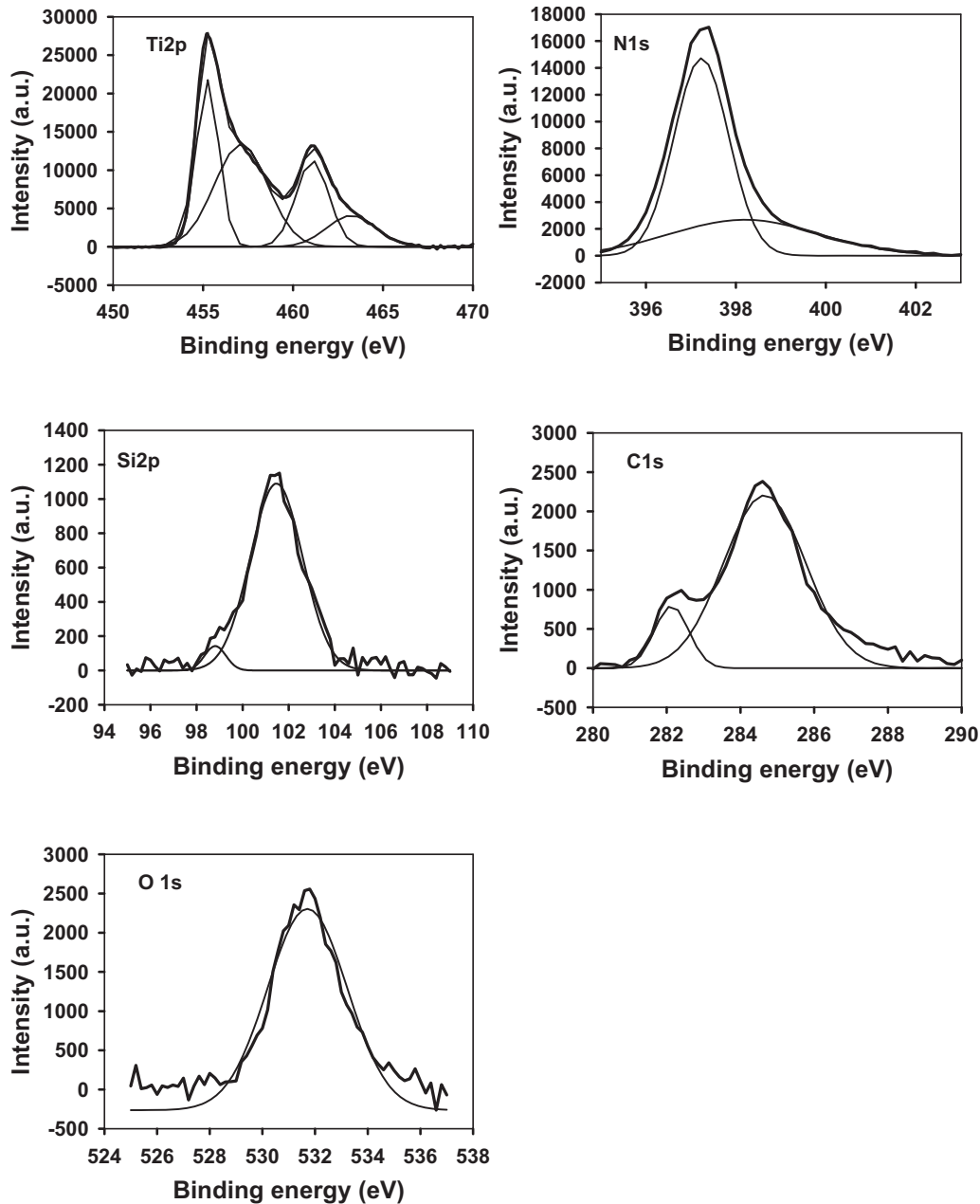
FIG. 4. Deconvolution of the high-resolution Ti 2p, N 1s, Si 2p, C 1s, and O 1s XPS spectra of the TiSiN coatings.

The Ti 2p spectrum is characterized with two main peaks at binding energies of 455.3 and 461.1 eV, respectively, in the binding energy range of 453–467 eV. In addition, two shoulder peaks at binding energies of 457.1 and 463.2 eV, respectively, can be distinguished from the two main peaks. Four Gaussian peaks were used to deconvolute the XPS Ti 2p spectra of the TiSiN coatings. The Ti 2p peak is composed of spin doublets, each separated by 5.8 eV. The first main peak and its shoulder peak correspond to the 2$p_{3/2}$ splitting, and the second main peak and its shoulder peak are their respective 2$p_{1/2}$ splitting.[16] It is well accepted that the two main peaks correspond to TiN phase. However, there is some debate about the origin of the two shoulder peaks. It has been reported that the shoulders observed on the high binding energy side of the Ti 2$p_{3/2}$ and Ti 2$p_{1/2}$ component peaks are inherent characteristic features of stoichiometric TiN, which attributed to the low-intensity loss peaks associated with the N 1s transition.[17,18] However, the shoulder peaks were also ascribed to the intermediate phases such as Ti$_2$O$_3$ or oxynitrides by some researchers.[19,20] According to the fitting results, the area ratio of the first peak and its shoulder peak is 0.69. If the shoulder peaks come from the intermediate phases, then most of the Ti atoms in the coatings exist as intermediate phases, which is not consistent with the O 1s spectrum results as discussed below. This indicates that the shoulder peaks are inherent characteristic features of the TiN phase.

The N 1s XPS spectrum exhibits a nearly symmetric peak at 397.23 eV with a weak shoulder at 398.2 eV in the binding energy range of 395–402 eV, which is slightly higher than that in the N 1s spectra of stoichiometric TiN (396.8 eV). Our previous XPS results on the TiN coatings deposited by a double bend filtered cathodic vacuum arc showed that the similar N 1s peak centered at 397.4 eV, and attributed to the upshift of the peak to the synergistic effect of the oxygen and titanium atoms in the coatings.[21] As the N 1s binding energy for Si–N has values between 397 and 398 eV, the existence of the Si–N bonds in the TiSiN coatings will also contribute to the upshift of the N 1s peak and the appearance of the shoulder peak at the high binding energy.[17] However, due to the much lower Si content as compared to the Ti content in the coatings, it is not possible to separate the N 1s component of the N–Si bonds from the N 1s spectrum. This indicates the existence of N–Ti bonds, N–Si bonds, and N–O–Ti bonds in the TiSiN coatings with most of the N atoms in the coating bonded to Ti atoms.

The Si 2p spectrum of the TiSiN coatings depicts a narrow and symmetric peak in the binding energy range of 98–104 eV. It is worth noting that a very weak shoulder at low binding energy can be distinguished. The Si 2p line was fitted using two Gaussian peaks at 98.8 (FWHM=0.93 eV) and 101.47 eV (FWHM=2.27 eV). The peak at 101.47 eV is believed to originate from Si 2p in amorphous silicon nitride (a-Si$_3$N$_4$), in which Si bonding coordination is tetrahedral (fourfold with N).[22] The peak at 98.8 eV is assigned to TiSi$_2$ or to free Si,[23] which accounts for 5% of the Si peak area. In the present case, the low deposition temperature limits the diffusion of Si atoms in the coatings, leading to the incomplete segregation of Si into TiN and a-Si$_3$N$_4$, therefore, the formation of some titanium silicides. The Si 2p spectrum shows that there are two kinds of phases, a-Si$_3$N$_4$ and TiSi$_2$, in the TiSiN coatings, but 95% of the Si atoms exist in a-Si$_3$N$_4$.

The C 1s spectrum exhibits a broad peak in the binding energy range of 280–290 eV. Careful inspection shows clearly a shoulder peak at the low binding energy range. As a result, the C 1s spectra were fitted with two peaks at a binding energy of 284.6 and 282.13 eV, respectively. The main Gaussian peak is at 284.6 eV with a FWHM of 2.24 eV, which accounts for 87% of the C 1s peak area. This peak is assigned to the C–C bonds originated from the adventitious carbon. The second peak, covering 23% of the peak area, is at 282.1 eV with a FWHM of 0.93 eV, which is very close to the C 1s binding energy (281.9 eV) of Ti–C bonds, and can be assigned to the Ti–C bonds.[24] This indicates that a small fraction of Ti–C phase exists in the TiSiN coating. The O 1s signal can be fitted with one Gaussian function at 531.7 eV, which corresponds to the O–Ti bonds in the coatings. As Ar plasma cleaning significantly reduces the C and O signals, most of the C and O atoms in the coatings originate from the contamination of the sample when exposed to the ambient environment. However, the origin of C–Ti bonds and partial O–Ti bonds in the coatings are believed to result from the
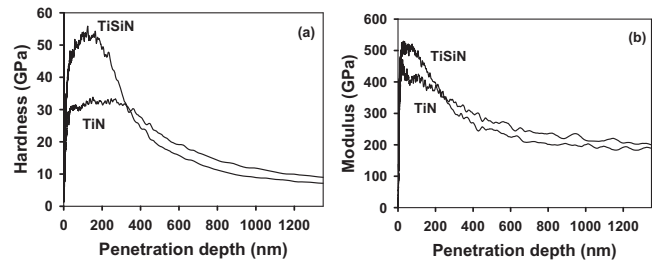

FIG. 5. (a) Hardness and (b) Young's modulus of the TiN and TiSiN coatings as a function of the penetration depth of the diamond tip.

contamination of the vacuum chamber by the oil vapors from the diffusion pump due to the high chemical reactivity of the Ti, C, and O ions in the arc plasma.

The mechanical properties of the TiN and TiSiN coatings deposited by using the same LAFAD system were ascertained by nanoindenter. Figure 5 shows the typical (a) hardness and (b) Young's modulus of the TiN and TiSiN coatings on 316 stainless steel as functions of the penetration depth of the diamond tips. All curves exhibit a similar variation trend with increasing penetration depth, which increase steeply, reaching the maximum, maintaining the same maximum hardness, followed by a gradual decrease in the measured hardness and Young's modulus with the further increase in the penetration depth. The initial rapid increase in the measured hardness and Young's modulus results from the size effect of the diamond tip, which is not an ideal sharp point.[25] The gradual decrease in the measured hardness and Young's modulus at a penetration depth of above 250–300 nm is attributed to the elastic and plastic deformation of the soft substrate under the high load of the indenter.

Data in Fig. 5 indicate that the maximum hardness of TiSiN coating is much higher than that of the TiN coating, but Young's modulus of the TiSiN coating is moderately higher than that of the TiN coating. The effective hardness and Young's modulus of the coatings can be calculated by averaging the hardness and Young's modulus in the penetration depth of 5%–10% of the coating thickness. For each coating, five measurements were performed. The averaged effective hardness and Young's modulus of the TiN and TiSiN coatings were computed to be 33, 376, 51, and 449 GPa. It is interesting to note that the hardness over Young's modulus (H/E) ratio (0.113) of TiSiN coatings is much higher than that (0.088) of the TiN coatings. For the tribological applications of the hard coatings, the high H/E ratio is very important for providing better wear resistance. The high H/E ratio of the TiSiN coatings may benefit their wear properties. In addition, the measured hardness and Young's modulus of the TiSiN coatings at larger penetration depth is smaller than that of the TiN coatings, which results from the smaller thickness of the TiSiN coatings (2.5 μm) than that of the TiN coatings (3 μm).

The load-displacement curve not only provides information about hardness and Young's modulus but also the plasticity and toughness of the hard coatings. Load-displacement measurements at a constant maximum load of 10 mN were
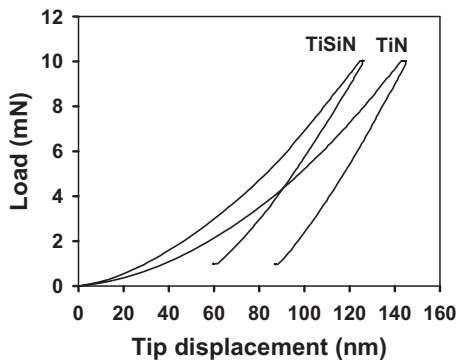
FIG. 6. Load-displacement curves of TiN and TiSiN coatings deposited by LAFAD.

conducted on TiSiN and TiN coatings. Figure 6 shows the typical load-displacement curves for TiSiN and TiN coatings at a maximum load of 10 mN. Clearly, we can see that at the same maximum load of 10 mN, the maximum displacement of the diamond tip on TiSiN coatings (125 nm) is much smaller than that of the TiN coatings (145 nm), indicating higher hardness and Young's modulus of TiSiN coatings. In addition, the load-displacement curves provide plastic deformation information of the hard coatings. Plasticity is defined as the ratio of the plastic displacement over the total displacement in the load-displacement curve:[26,27] plasticity $= \varepsilon_p / \varepsilon = D_r / D_{max}$, where ε_p is the plastic deformation, ε is the total deformation, D_r is the retained depth of the diamond tip after completely unloading the load, and D_{max} is the penetration depth of the diamond tip at maximum load. The plasticity of the TiSiN and TiN coatings was calculated to be 51% and 59%, respectively. It is worth noting that TiSiN coatings possess much higher hardness than TiN coatings but similar plasticity. As plastic deformation leads to stress relaxation in materials, higher plasticity corresponds to the easier stress relaxation process, and therefore, higher toughness of the materials. The high hardness and high plasticity of the TiSiN coatings are crucial for practical applications.

IV. DISCUSSION

It is well accepted that nanocomposite TiSiN coatings consisting of isolated nanosized TiN grains covered with amorphous Si_3N_4 monolayer are synthesized by spinodal phase segregation. Veprek et al.[2–4] proposed that in a Ti–Si–N system, spinodal phase segregation is thermodynamically driven by a high activity of nitrogen and rate-controlled by diffusion that requires a sufficiently high temperature. According to his hypothesis, sufficiently high nitrogen partial pressure (>1 Pa) and deposition temperature (>500 °C) are needed to provide the necessary thermodynamic driving force for spinodal decomposition to occur during the deposition of nanocomposite coatings.

In the present study, during the deposition of nanocomposite TiSiN coatings, the nitrogen partial pressure (0.02 Pa) and deposition temperature (>350 °C) are significantly lower than that required by Veprek's model. However, XRD and XPS results clearly indicate that the deposited TiSiN

coatings are nanocomposite coatings, consisting of TiN nanocrystals (5.8 nm in diameter) and amorphous Si_3N_4 phase. We know that cathodic arc discharge is a low voltage and high current electric discharge between two electrodes in a vacuum environment. The extremely high power density in the arcing spot area generates high local temperature, which evaporates the target materials and emits large amounts of electrons and ions. The characteristic of cathodic arc is the high ionization rate (>90%) and high ion energy. When N_2 gas was introduced into the deposition chamber, N_2 molecules were ionized by the low energy electrons, which formed dense plasma with an ionization efficiency of as high as 30%. It is well known that the nitrogen ions and the neutral nitrogen atoms in the plasma have remarkable activity. As a result, a small amount of reactive nitrogen specials are needed in the cathodic arc plasma to provide the required nitrogen activity for the deposition of the nanocomposite TiSiN coatings.

In addition, during coating deposition, the growing coating surface was bombarded by energetic Ti and N ions, which were attracted by negative substrate bias (−40 V). The energy of Ti ions bombarding the growing coating surface has been calculated to be 147.6 eV in our previous paper.[13] The collision of energetic Ti and N ions with the growing coating surface transfers most of their energy to the atoms on the coating surface, which significantly improves their mobility on the coating surface. Furthermore, our filtered cathodic arc is a high rate deposition technique; the ion current density of the current deposition system was measured to be 5 mA/cm². The high ion energy as well as the high ion current density of the filtered cathodic arc plasma provides the energy needed for the spinodal phase segregation in TiSiN coatings, leading to the formation of nanocomposite TiSiN coatings at a much lower deposition temperature. Anders[28] and Musil[29] also proposed that the bombardment of energetic ions caused an atomic scale heating (ASH) effect to the growing coating and the ASH can replace conventional heating to produce dense films.

It is interesting to note that by adding Si atoms into TiN coatings, the preferred orientation of TiN grains change from strong (111) preferred orientation to fully (220) preferred orientation. Most of the TiN coatings deposited by physical vapor deposition or chemical vapor deposition exhibit strong (111) or (200) preferred orientations, depending on the deposition technique and process. The formation of preferred orientation in the films has been explained by a few models in terms of strain energy, surface energy, and kinetic factors.[30,31] It was proposed that the coating grows toward (111) plane when the strain energy is dominated, toward (200) orientation when the surface energy is dominated, and toward (110) orientation at intermediate stress.[32] However, neither of these models is appropriate for the nanocomposite TiSiN coatings deposited by LAFAD.

The change in preferred orientation of TiN coatings from (111) to (220) by adding Si atoms could be explained by the low mobility of the Ti and Si atoms on the coating surfaces. The formation of (111) preferred orientation for TiN coatings

is believed to result from the high internal stress in the deposited coatings to minimize the strain energy. However, for the deposition of nanocomposite TiSiN coatings, during the spinodal phase transformation, Si atoms have to diffuse to the grain boundary, whereas the strong bonds formed between Si atoms and Si, Ti, and N atoms hinder the diffusion of Si and Ti atoms. In addition, the low deposition temperature also hinders the long range diffusion of the Si and Ti atoms on the growing coating surface. Although the thermal spike formed by the bombardment of energetic ions can improve the atom mobility, the effect of thermal spike is in a very short range. The low mobility of the Ti and Si atoms leads to the growth of coatings along a less dense plane. For a cubic crystal with face centered cubic (fcc) structure, the three basal planes are (100), (110), and (111). The planar densities of the (110), (100), and (111) are calculated to be about $1.41/a^2$, $2/a^2$, and $2.31/a^2$ atoms/unit area, where a is the lattice constant. Therefore, for fcc crystals, the (110) plane has the lowest planar density, and is the most open basal plane. This explains the formation of the (220) preferred orientation for TiSiN coatings deposited by LAFAD.

The spinodal nature of the phase segregation in the TiSiN coatings corresponds to the formation of unique nanocomposite microstructure consisting of nanosized TiN grains encapsulated in amorphous Si_3N_4 layers. As proposed by Veprek et al.,[2–4] the dislocations are absent in 3–6 nm small nanocrystals, in which the plastic deformation mechanism changes from dislocation sliding to grain boundary sliding. However, in TiSiN coatings, the high bonding energy of Si–N and Si–Ti bonds in the grain boundary hindered the grain sliding, corresponding to the super high hardness of the TiSiN coatings deposited by LAFAD technique.

V. CONCLUSIONS

In this study, a LAFAD deposition technique was used to deposit nanocomposite TiSiN coatings at a low temperature (350 °C) and low N_2 partial pressure (0.02 Pa) from TiSi alloy targets with 20 at. % Si. XRD results indicate that by adding Si atoms into TiN coatings, the grain size significantly reduced from 16.9 to 5.8 nm, and the growing orientation changes from strong (111) preferred orientation to fully (220) preferred orientation. XPS results show that the atomic ratio of Si over Ti atoms in the deposited TiSiN coatings is 0.17, and both TiN and Si_3N_4 phases exist in the coatings. Nanoindentation results indicate that the TiSiN coatings possess much higher hardness (51 GPa) and Young's modulus (449 GPa) than those of the TiN coatings (33 and 376 GPa, respectively). Both XRD and XPS results imply that the deposited TiSiN coating is a nanocomposite coating, consisting of nanosized TiN grains encapsulated by amorphous Si_3N_4 layer. The nanocomposite nature of the TiSiN coatings corresponds to the ultrahigh hardness of the TiSiN coatings.

[1] J. Musil, Surf. Coat. Technol. **125**, 322 (2000).
[2] S. Veprek and M. G. J. Veprek-Heijman, Surf. Coat. Technol. **201**, 6064 (2007).
[3] S. Veprek, A. Niederhofer, K. Moto, T. Bolom, H.-D. Mannling, P. Nesladek, G. Dollinger, and A. Bergmaier, Surf. Coat. Technol. **133–134**, 152 (2000).
[4] S. Veprek, M. G. J. Veprek-Heijman, P. Karvankova, and J. Prochazka, Thin Solid Films **476**, 1 (2005).
[5] Y. C. Ee, Z. Chen, W. D. Wang, D. Z. Chi, S. Xu, and S. B. Law, Surf. Coat. Technol. **198**, 291 (2005).
[6] Z. G. Li, Y. X. Wu, and S. Miyake, J. Vac. Sci. Technol. A **25**, 1524 (2007).
[7] C. T. Guo, D. Lee, and P. C. Chen, Appl. Surf. Sci. **254**, 3130 (2008).
[8] S. M. Yang, Y. Y. Chang, D. Y. Lin, D. Y. Wang, and W. Wu, Surf. Coat. Technol. **202**, 2176 (2008).
[9] V. I. Gorokhovsky, V. P. Polistchook, and I. M. Yartsev, Surf. Coat. Technol. **61**, 101 (1993).
[10] S. Mitura, Z. Has, and V. Gorokhovsky, Surf. Coat. Technol. **47**, 106 (1991).
[11] V. I. Gorokhovsky, D. G. Bhat, and R. Bhattacharya, Surf. Coat. Technol. **140**, 215 (2001).
[12] V. Gorokhovsky, U.S. Patent No.6,663,755 B2 (Dec. 16, 2003).
[13] Y. H. Cheng, T. Browne, B. Heckerman, J. C. Jiang, E. I. Meletis, C. Bowman, and V. Gorokhovsky, J. Appl. Phys. **104**, 093502 (2008).
[14] JCPDS Card No. 65-3597.
[15] JCPDS Card No. 65-0965.
[16] A. Vesel, M. Mozetic, J. Kovac, and A. Zalar, Appl. Surf. Sci. **253**, 2941 (2006).
[17] I. Bertoti, Surf. Coat. Technol. **151–152**, 194 (2002).
[18] M. Guemmaz, A. Moser, and J. C. Parlebas, J. Electron Spectrosc. Relat. Phenom. **107**, 91 (2000).
[19] J. Halbritter, H. Leiste, H. J. Mathes, and P. Walk, Anal. Chem. **341**, 320 (1991).
[20] F. H. Lu and H. Y. Chen, Surf. Coat. Technol. **130**, 290 (2000).
[21] Y. H. Cheng and B. K. Tay, J. Vac. Sci. Technol. **21**, 1609 (2003).
[22] S. Veprek, J. Vac. Sci. Technol. A **17**, 2401 (1999).
[23] J. Perez-Mariano, K.-H. Lau, A. Sanjurjo, J. Caro, D. Casellas, and C. Colominas, Surf. Coat. Technol. **201**, 2217 (2006).
[24] M. A. Baker, Surf. Coat. Technol. **201**, 6105 (2007).
[25] C. Charitidis and S. Logothetidis, Thin Solid Films **482**, 120 (2005).
[26] Y. V. Milman, B. A. Galanov, and S. I. Chugunova, Acta Metall. Mater. **41**, 2523 (1993).
[27] S. Zhang, D. Sun, Y. Fu, and H. Du, Surf. Coat. Technol. **198**, 74 (2005).
[28] A. Anders, Appl. Phys. Lett. **80**, 1100 (2002).
[29] J. Musil, Surf. Coat. Technol. **125**, 322 (2000).
[30] J. E. Greene, J.-E. Sundgren, L. Hultman, I. Petrov, and D. B. Bergstrom, Appl. Phys. Lett. **67**, 2928 (1995).
[31] J. Pelleg, L. Z. Zevin, S. Lungo, and N. Croitoru, Thin Solid Films **197**, 117 (1991).
[32] Y. H. Cheng and B. K. Tay, J. Cryst. Growth **252**, 257 (2003).